AGU100 ADVANCING EARTH AND SPACE SCIENCE

Geophysical Research Letters

RESEARCH LETTER
10.1029/2020GL087530

Poloidal- and Toroidal-Mode Mantle Flows Underneath the Cascadia Subduction Zone

Hejun Zhu[1,2], Xueyan Li[1], Jidong Yang[1], Robert J. Stern[1], and David E. Lumley[1,2]

[1]Department of Geosciences, The University of Texas at Dallas, Richardson, TX, USA, [2]Department of Physics, The University of Texas at Dallas, Richardson, TX, USA

Abstract Several hypotheses have been proposed to explain intriguing circular shear wave splitting patterns in the Pacific Northwest, invoking either 2-D entrained flows or 3-D return flows. Here, we present some hitherto unidentified, depth-dependent anisotropic signatures to reconcile different conceptual models. At depths shallower than 200 km, the fast propagation directions of seismic waves to the west of the Rocky Mountain are aligned sub-parallel to the subduction direction of the Juan de Fuca and Gorda Plates. This pattern is consistent with previous onshore/offshore shear wave splitting measurements and indicates that 2-D entrained flows dominate at shallower depths. From 300 to 500 km, two large-scale return flows are revealed, one circulating around Nevada and Colorado and the other running around the edge of the descending Juan de Fuca slab. These observations suggest the development of toroidal-mode mantle flows, driven by the fast rollback of the narrow, fragmented Juan de Fuca and Gorda slabs.

Key Points:
- The fast directions are aligned sub-parallel to the subduction direction of the Juan de Fuca Plates at depths shallower than 200 km
- Two large-scale return flows are revealed, circulating around the edges of the descending Juan de Fuca and Gorda slabs
- The uppermost lower mantle beneath the Cascadian Subduction Zone is dominated by a NE-SW oriented flow field

Supporting Information:
- Supporting Information S1

Correspondence to:
H. Zhu,
hejun.zhu@utdallas.edu

Citation:
Zhu, H., Li, X., Yang, J., Stern, R. J., & Lumley, D. E. (2020). Poloidal- and toroidal-mode mantle flows underneath the Cascadia Subduction Zone. *Geophysical Research Letters*, *47*, e2020GL087530. https://doi.org/10.1029/2020GL087530

Received 14 FEB 2020
Accepted 4 MAY 2020
Accepted article online 16 MAY 2020

1. Introduction

The Cascadia Subduction Zone (CSZ) is a hot and young (<25 Myr) end-member of global subduction systems. From north to south along the western coast of the United States and Canada, the CSZ involves the sinking of the young Explorer, Juan de Fuca and Gorda slabs underneath the North American Plate. It is now bounded by the Mendocino Triple Junction (MTJ) to the south and the Queen Charlotte Fault System (QCFS) to the north (Figure 1). The forearc of this active convergent margin is limited to the east by the Cascade Volcanic Chain, and the Rocky Mountain Front (RMF) is considered as the eastern boundary of its back-arc region. Currently, in a hotspot reference frame, the Juan de Fuca Plate is moving toward northeast at a speed of 41 mm/yr, the Pacific Plate to the south of the MTJ is moving toward northwest at 49 mm/yr, and the overriding North American Plate is moving toward southwest at 14–26 mm/yr (Gripp & Gordon, 2002). The Explorer, Juan de Fuca and Gorda Plates are considered as the northern remnants of the ancient Farallon Plate, which has been subducted underneath North America since the Mesozoic (Atwater & Stock, 1998). The CSZ is an interesting location to study the dynamics of subduction processes, because it involves the fast rollback (30 mm/yr) Juan de Fuca and Gorda slabs (Schellart et al., 2008), which might be fragmented along the strike (Hawley & Allen, 2019; James et al., 2011; Obrebski et al., 2010; Sigloch et al., 2008). In addition, the Cenozoic arc volcanisms of the CSZ exhibit complex patterns in isotope signatures, as documented in the Columbia River Flood Basalts, and bifurcate High Lava Plains (HLP) and Snake River Plain (SRP) (Camp & Ross, 2004; Ford et al., 2013). These geochemical and geophysical characteristics might be the surface manifestations of complicated, deep mantle flows underneath the CSZ.

Shear wave splitting (SWS) measures the birefringence of seismic wave energy passing through intrinsically anisotropic minerals, such as olivine and orthopyroxene in the upper mantle, or through stress-induced regions (Gavin & Lumley, 2016). It has been widely considered as an important proxy for characterizing present-day mantle flows, "frozen-in" lithospheric deformation as well as stress orientations, given the relation between shear strain and the lattice-preferred orientation (LPO) of anisotropic mineral aggregates (Zhang & Karato, 1995). To date, a variety of SWS patterns have been documented in the Pacific Northwest (PNW). For instance, both Currie et al. (2004) and Eakin et al. (2010) have reported that SWS patterns are sub-parallel to the absolute plate motion direction of the Juan de Fuca Plate in the arc region, in agreement with the conceptual 2-D corner flow model in the mantle wedge, entrained by the downgoing slabs (Hall et al., 2000). Such a poloidal-mode pattern, that is, trench-perpendicular, extends to the offshore Cascadia based on measurements from recently deployed ocean bottom seismometers (Bodmer et al., 2015; Martin-Short et al., 2015). However, trench-parallel SWS patterns have neither been observed in the sub-slab

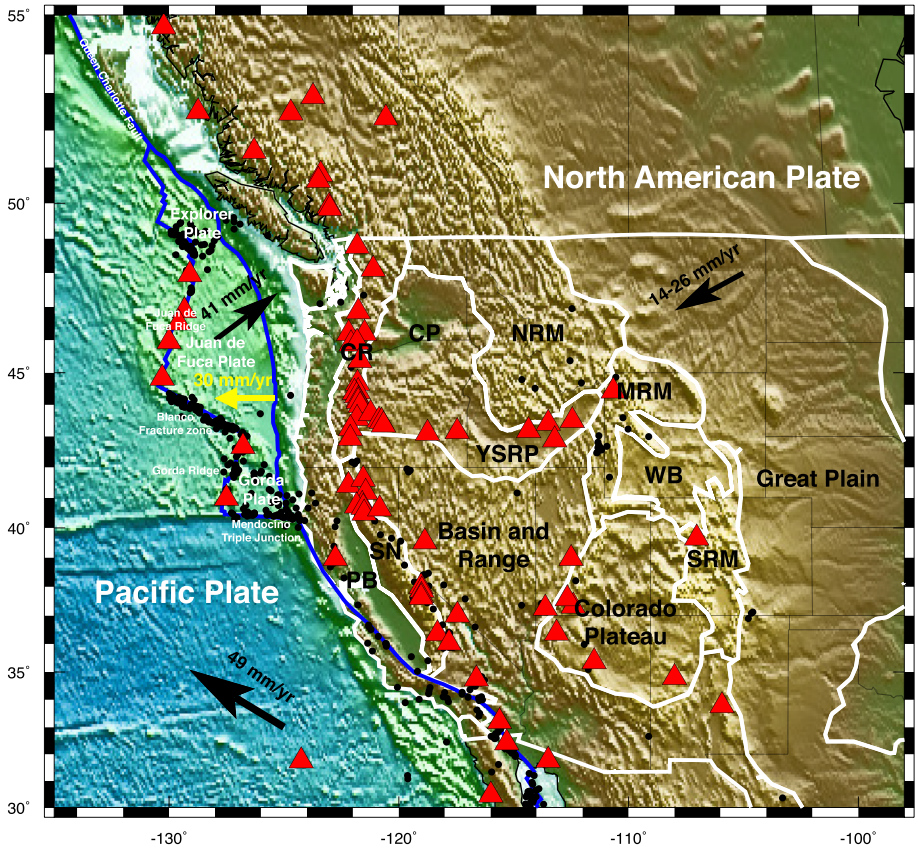

Figure 1. Tectonic map for the western United States and Canada. Blue lines denote the global plate boundaries (Bird, 2003). Red triangles represent the Cenozoic volcanoes (www.ngdc.noaa.gov/hazard), and black dots show the distribution of earthquakes with magnitude greater than 5. Black arrows denote plate motion directions (Gripp & Gordon, 2002), and the yellow arrow shows the trench migration velocity of the CSZ (Schellart et al., 2007), all with the Pacific hotspot reference frame. Abbreviations for major tectonic provinces are as follows: CP = Columbia Plateau; CR = Cascade Range; MRM = Middle Rocky Mountain; NRM = Northern Rocky Mountain; PB = Pacific Border; SN = Sierra Nevada; SRM = Southern Rocky Mountain; WB = Wyoming Basin; YSRP = Yellowstone-Snake River Plain.

nor fore-arc regions (Long, 2016), making the CSZ a unique place to study in comparison to other subduction systems (Long & Silver, 2008; Russo & Silver, 1994; Smith et al., 2001). Furthermore, a striking, circular SWS pattern was observed to the south of the MJT, with its center around the Great Basin of Nevada (Savage & Sheehan, 2000). To date, several conjectures have been proposed to explain its origins. For instance, based on the collocation of the minimum SWS time with a fast wave speed anomaly at 200 km underneath central Nevada, this circular pattern was interpreted as the surface expression of a deep transient lithospheric drip (West et al., 2009). In contrast, Savage and Sheehan (2000) suggested its connection with an underlying mantle plume, and Stern and Dumitru (2019) argued that might result from a fossil Eocene plume head. Moreover, Zandt and Humphreys (2008) postulated the occurrence of toroidal-mode mantle flows surrounding the southern edge of the Gorda slab and moving through the slab fragmentations, offering us another explanation for this intriguing circular SWS pattern. These controversial interpretations reflect the limited vertical resolution of SWS observations, since they represent the integrated effect of seismic anisotropy over the entire wave path (Silver, 1996). Here, by examining depth-dependent azimuthal anisotropy in a new tomographic model US_{32}, we attempt to reconcile these hypotheses and better characterize the mantle flow field underneath the CSZ.

2. Methods

Model US_{32} was constructed by using full waveform inversion (Fichtner et al., 2009; Tape et al., 2009; Tarantola, 1984; Tromp et al., 2005), with temporary and permanent seismic networks, including the USArray, deployed in North and Middle America. The current data set consists of 180 regional earthquakes,

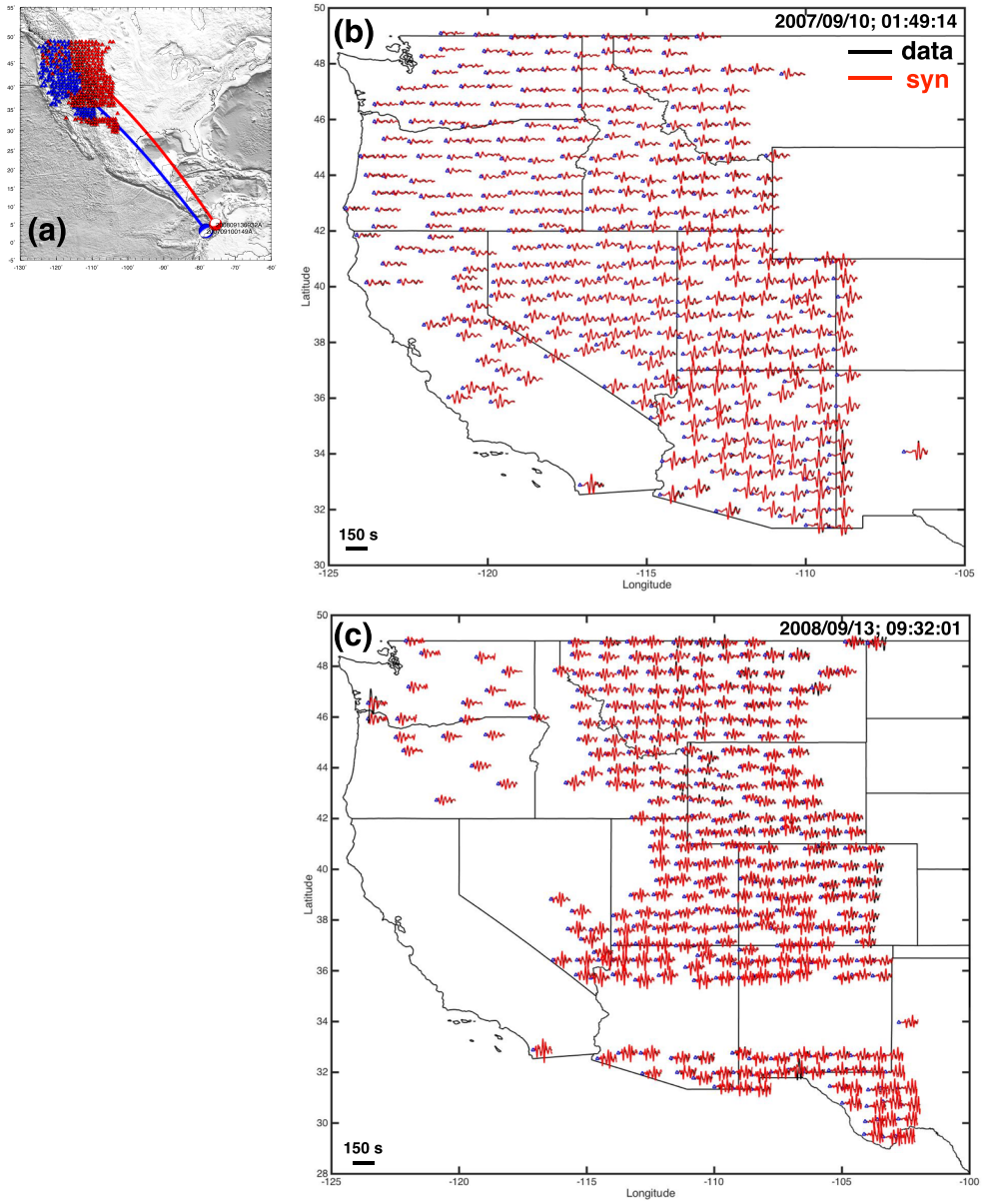

Figure 2. Comparisons of radial-component, observed (black) and predicted (red) seismograms for two earthquakes occurred in Colombia. Panel (a) shows the locations of the shallow earthquake CMTSOLUTION_200709100149A (blue), and the deep earthquake CMTSOLUTION_200809130932A (red), as well as their responded TA stations denoted by blue and red triangles, respectively. Panel (b) compares direct S waveforms for 346 TA stations, responded to the shallow event. Panel (c) shows waveform comparisons for both direct S waves and depth phase sS for 314 TA stations, responded to the deep event. A 150-s window after the theoretical S arrival time for the PREM model (Dziewonski & Anderson, 1981) is used for both cases. Predictions and observations are band-pass filtered from 15 to 40 s.

occurred from 2003 to 2013, with magnitudes ranging from 4.5 to 6.5 and recorded by 4,516 seismographic stations. Three-component predicted seismograms are calculated by solving the anisotropic/anealstic wave equation using the spectral-element approach (Komatitsch & Tromp, 1999; Peter et al., 2011). These predictions are then compared with observed seismograms, and their discrepancies are quantified by frequency-dependent phase measurements (Laske & Masters, 1996; Zhou et al., 2004). Three-component short-period (15–40 s) body waves and long-period (25–100 s) surface waves are combined to jointly constrain deep and shallow structures (Zhu et al., 2012). Over the course of inversion, the crustal and mantle structures are simultaneously updated to avoid the usage of crustal correction (Lekic et al., 2010). The current model is the result of 32 preconditioned conjugate gradient iterations (Fletcher & Reeves, 1964) and was

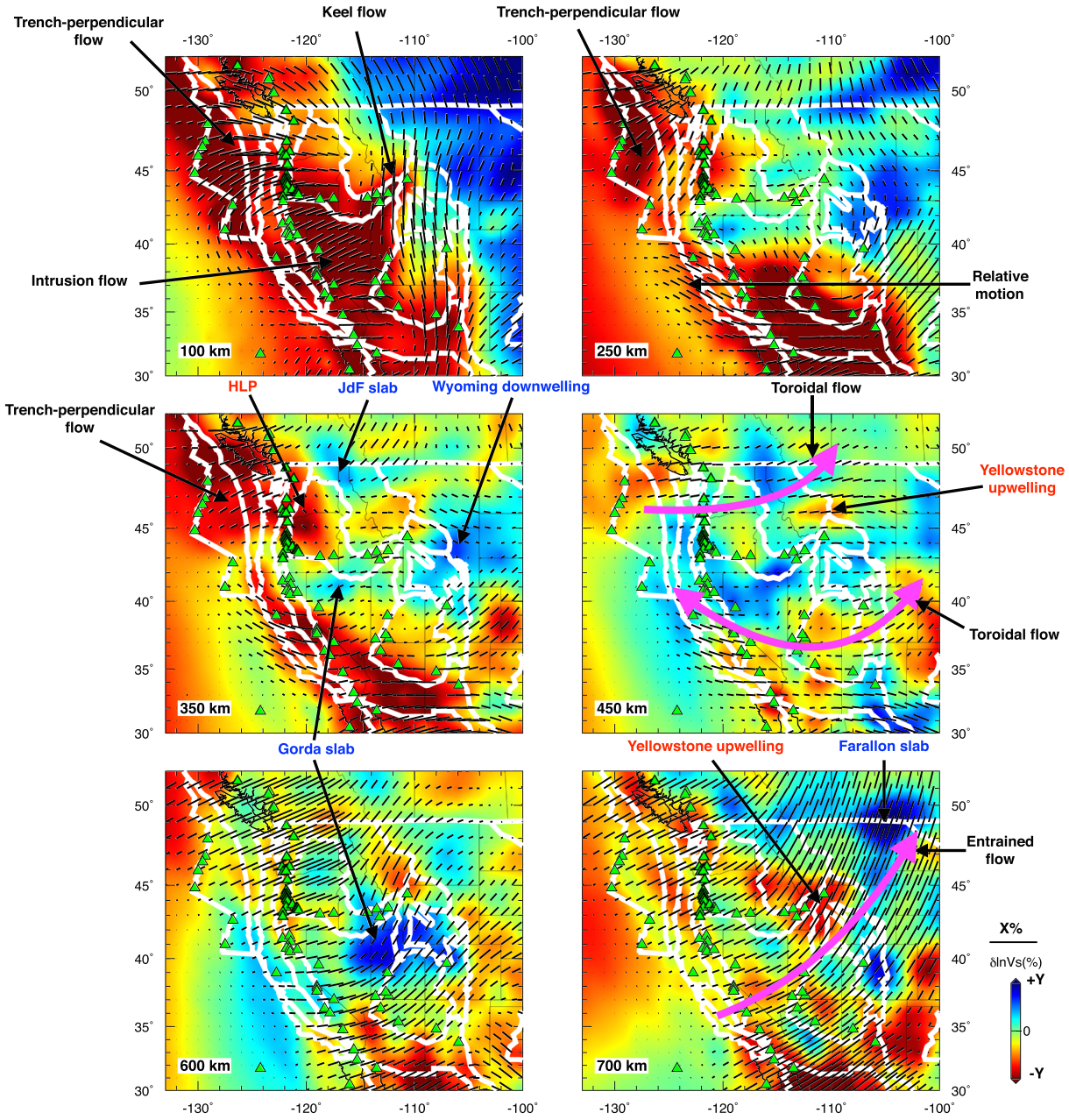

Figure 3. Horizontal depth slices of relative perturbations in isotropic shear wave speed and azimuthal anisotropy at depths ranging from 100 to 700 km in model US_{32}. The 1-D reference model STW105 (Kustowski et al., 2008) is used to calculate relative wave speed perturbations. The direction and magnitude of the fast axes are given by the orientation and length of the black bars. Key features discussed in the main text are highlighted by arrows. Magenta curves at 450 and 700 km are used to highlight two large-scale, toroidal-mode mantle flows, as well as entrained flows, respectively. White lines denote the global plate boundaries (Bird, 2003) and tectonic provinces, and green triangles represent the Cenozoic volcanoes. The anisotropic strength X = 3 and wave speed magnitude Y = 6% for the depth slice at 100 km, X = 1 and Y = 2% for the rest of depth slices.

constrained by 586,185 phase measurements. Both radially and azimuthally anisotropic model parameters, including L, N, G_c, and G_s, are simultaneously updated (Debayle et al., 2016; Schaeffer et al., 2016), based on their misfit gradients calculated by the adjoint state method (Sieminski et al., 2007a, 2007b). Details about the construction of model US_{32} can be found in Zhu et al. (2020).

Figure 2 compares radial component, observed (black) and predicted (red) seismograms from model US_{32} for two earthquakes occurred underneath Colombia, and recorded by the USArray deployed in the western United States in 2007 and 2008. Both data and predictions are band-pass filtered from 15 to 40 s, and here we only present waveform fittings for S and sS phases. More waveform comparisons for three-component body

and surface waves can be found in the supporting information Figures S1–S5. The first event (CMTSOLUTION_200709100149A) was a M_w 6.1 earthquake that occurred at a depth of 16.7 km, and the second event (CMTSOLUTION_200809130932A) was a deep (132.7 km) earthquake with moment magnitude of 5.9. A 150-s window after the theoretical direct S arrival time from the PREM model (Dziewonski & Anderson, 1981) is used for these comparisons. For the first shallow event, the direct S waveforms are matched very well for all 346 TA stations deployed to the west of the RMF, with the average cross-correlation coefficient around 0.895. For the second deep event, well-developed sS phases are separated from direct S arrivals, and both of them are fitted very well for 314 TA stations, with the average cross-correlation coefficient around 0.755. These good waveform fittings suggest that the mantle structures underneath the western United States are well constrained in model US_{32}. The highest frequency used in the inversion is 15 s; therefore, the minimum wavelength reaches to 60 to 75 km, and the nominal resolution can reach to 30 to 40 km depending on the ray sampling. Detailed resolution and illumination analysis of model US_{32} in the western United States can be found in the supporting information Figures S6–S9.

3. Results

3.1. Poloidal-Mode Mantle Flows at Shallow Depths

Figures 3–5 present map views, vertical slices, and 3-D iso-surface representation of the current model US_{32} in the PNW. More uninterpreted cross sections can be found in the supporting information Figure S10. At depths shallower than 200–250 km, the western United States is dominated by strong slow wave speed anomalies (Figure 3), consistent with previous tomographic studies (supporting information Figure S11). Similar to the model derived from surface wave dispersions (Shen & Ritzwoller, 2016), the current model lacks narrow fast wave speed anomalies along the strike of the CSZ in Washington, Oregon, and Northern California (Burdick et al., 2013; Hawley & Allen, 2019; Obrebski et al., 2011; Schmandt & Humphreys, 2010; Schmandt & Lin, 2014); this is because the shallow structures in model US_{32} are mainly constrained by long-period surface waves (25–100 s), resulting in relatively poor horizontal resolution in comparison to body wave tomographic results, which are mainly constrained by short-period signals. Other prominent features include the finger-like anomalies along the strike of the SRP and around the Colorado Plateau. A sharp wave speed contrast between the western (slow) and eastern (fast) United States is delineated along the RMF. To its east, the North American lithosphere is characterized as a thick fast wave speed volume down to 200–250 km deep (Figure 4).

To the west of the RMF at these shallow depths, the fast directions are sub-parallel to subduction directions of the Juan de Fuca and Gorda Plates (Figure 3). For instance, beneath Cascadia, the fast axes rotate clockwise from NW to EW beneath the arc region, consistent with previous onshore and offshore SWS measurements (Bodmer et al., 2015; Currie et al., 2004; Eakin et al., 2010; Martin-Short et al., 2015). This pattern reflects entrained and corner flows, dominating in the sub-slab and mantle wedge at shallow depths, respectively. Such a trench-perpendicular pattern extends to the south beneath the Pacific coast and Basin and Range Province and follows the trajectory of the SRP down to 100 km. This might reflect the eastward intrusion of intraplate magma, induced by the subduction of the Farallon slab as demonstrated by mantle flow simulations (Zhou et al., 2018). Furthermore, there is a sharp transition in anisotropic fabrics across the RMF, turning from northeast-southwest to a north-south orientation underlying the Rocky Mountain. This transition correlates with wave speed heterogeneities and reflects the contrast between present-day asthenospheric flows beneath the western United States and "frozen-in" lithospheric deformation along the strike of the RMF.

3.2. Subduction-Induced Toroidal-Mode Mantle Flows at Greater Depths

From 300 to 700 km, model US_{32} exhibits a number of fast wave speed anomalies, corresponding to the descending Juan de Fuca, Gorda, and remnant Farallon slabs. For instance, to the north of 45°N, the Juan de Fuca slab dips toward east down to 400 km (Profile A-a in Figure 4). Prominent slow wave speed anomalies are revealed beneath the descending slab, which might suggest the accumulation of high viscosity materials in the sub-slab region (Hawley et al., 2016). In Cross Section A-a, a second fast anomaly is observed below the 660-km discontinuity, possibly representing the remnant Farallon slab in the uppermost lower mantle. Similarly, to the south of 45°N, the Gorda slab sinks toward east and flattens within the mantle transition zone (Profile B-b in Figure 4), with some leakage toward the lower mantle, which might result from tradeoffs between wave speeds and depth variations of the 660-km discontinuity. There is a gap between the Juan de

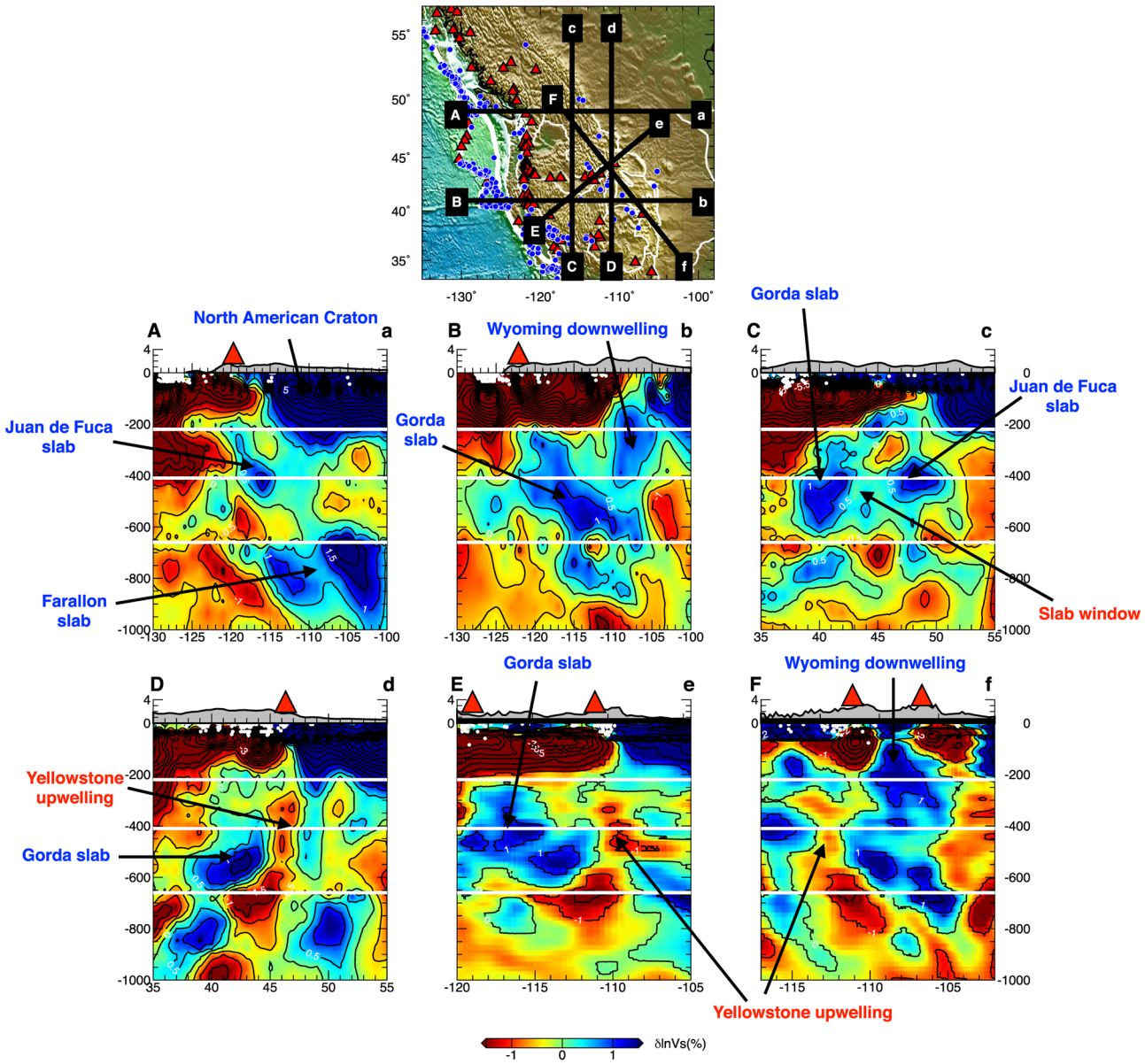

Figure 4. Vertical cross sections of relative perturbations in isotropic shear wave speed for the western United States in model US_{32}. The top panel shows the locations of six profiles in the bottom panel. The white lines in these vertical cross sections denote the 220-, 410-, and 660-km discontinuities. Earthquakes with magnitude greater than 5 are shown as white circles, and red triangles represent volcanoes.

Fuca and Gorda slabs around 45°N from 250 to 450 km (Figure 3 and Cross Section C-c in Figure 4), which was interpreted as a slab window due to the fragmentation of the Juan de Fuca and Gorda Plates (Hawley & Allen, 2019; James et al., 2011; Obrebski et al., 2010). This slab window is filled with slow anomalies at depths shallower than 400 km, which might be melt zones beneath the Newberry-HLP (Figure 3), and explain the lack of seismicity in central Oregon compared to the northern and southern CSZ (Figure 1). It appears that both the Juan de Fuca and Gorda slabs are detaching from the surface (supporting information Figure S12), which might explain the lack of well-developed Wadati-Benioff zone underneath the Cascadia convergent margin in comparison to other subduction systems (Gao, 2018). Moreover, there is an intriguing fast body down to 400 km beneath the Wyoming Craton (Profile B-b in Figure 4 and 3-D visualization in Figure 5). This feature has also been identified in previous body and surface wave tomographic models (Humphreys et al., 2015) and is more prominent than the postulated lithospheric downwelling underneath Nevada (West et al., 2009) and delamination underneath the Colorado Plateau (Levander et al., 2011). We interpret the Wyoming

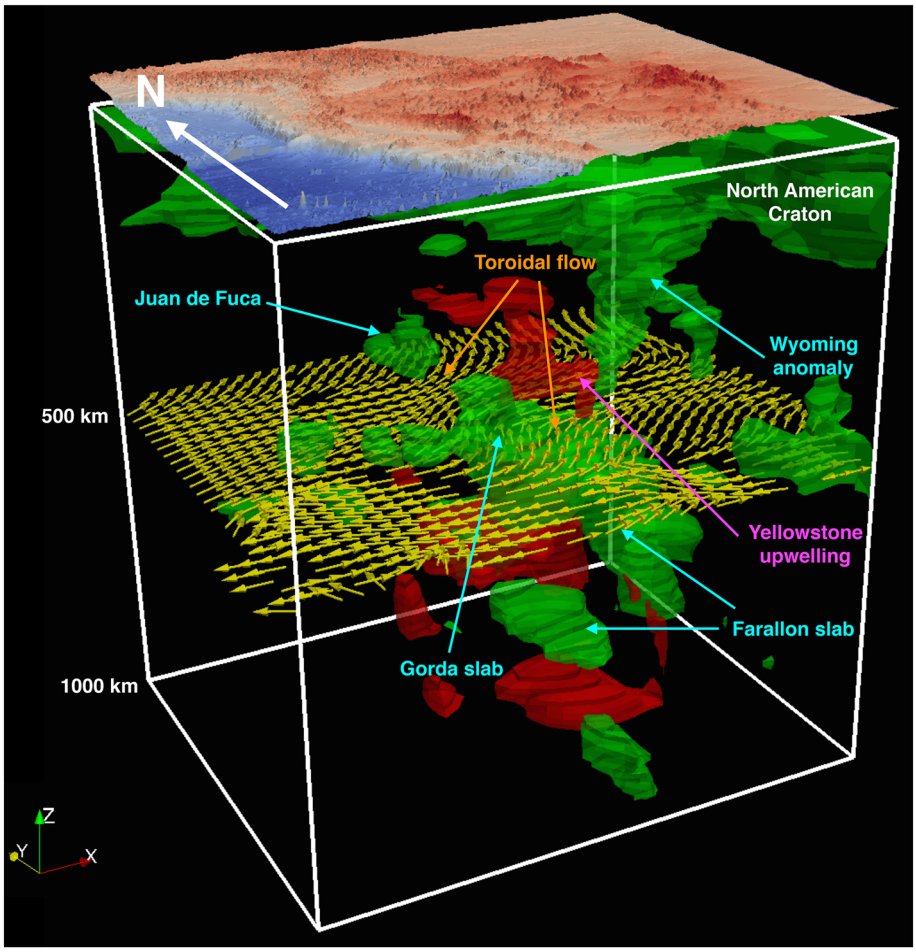

Figure 5. 3-D iso-surface representations of wave speed anomalies with magnitude greater than +1% (green bodies) and less than −0.8% (red bodies), as well as the fast axes (yellow arrows) at a depth of 500 km in model US_{32}. Topography is superimposed on top of the 3-D iso-surface bodies. Cyan arrows are used to highlight slab features while orange arrows are used to denote mantle flow fields.

feature as the edge-driven, small-scale downwelling due to the contact between the warm and tectonically active western United States, with the thick and cold North American Craton (King & Anderson, 1998).

At these depths, the trench-perpendicular, fast axis direction at shallow depths turns to two large-scale return flows (Figures 3 and 5). The first (Figure 3 at 450 km) follows the edge of the Gorda slab and Wyoming downwelling, clockwise rotating from NE-SW underneath Colorado, to east-west in Nevada, then align to NW-SE in California. The second rotating flow (Figure 3 at 450 km) surrounds the southern boundary of the Juan de Fuca Plate, acrossing the slab window around 45°N and moving NE. These results support the previous hypothesis about toroidal-mode mantle flows driven by the fast rollback (30 mm/yr) of the Juan de Fuca and Gorda slabs (Zandt & Humphreys, 2008). In particular, slab fragmentation around 45°N might facilitate the development of return flows due to the creation of lateral pressure gradients. In comparison to the Juan de Fuca slab, the sinking Gorda slab is larger in volume within the mantle and, therefore, imposes a stronger slab pull force, which might lead to larger toroidal-mode mantle flows around its edge. This may explain the presence of a circular SWS pattern in Nevada, instead of around the Juan de Fuca slab in Idaho and Montana. In the uppermost lower mantle (700 km), model US_{32} is dominated by a NE-SW oriented flow. This might reflect substantial shear strain produced when the Farallon slab penetrated the 660-km discontinuity to the lower mantle.

Profiles D-d to F-f in Figure 4 are used to examine the morphology of slow wave speed anomalies underneath the Yellowstone-SRP. A continuous slow wave speed anomaly with magnitude around −1% ascends from the mantle transition zone to the surface, in agreement with previous tomographic studies

(supporting information Figure S13) (James et al., 2011; Obrebski et al., 2010). It is surrounded by the Juan de Fuca and Gorda slabs, and the Wyoming downwelling, suggesting the close relation between the hot mantle upwelling and subduction processes. The current model US_{32} does not illuminate the lower mantle (supporting information Figures S6 and S7) well enough to address the debate on the deep origin of the Yellowstone plume (Nelson & Grand, 2018; Schmandt et al., 2012; Yuan & Dueker, 2005; Zhou, 2018; Zhou et al., 2018).

4. Discussion

Model US_{32} exhibits modest magnitude of azimuthal anisotropy within the mantle transition zone and uppermost lower mantle. By comparing with SWS measurements (Montagner et al., 2000; Yuan et al., 2011), the anisotropic strength in the current model might be underestimated (supporting information Figure S15), suggesting that stronger azimuthal anisotropy might exist in reality. Here, we only compare azimuth-averaged SWS measurements with azimuthal anisotropy in model US_{32}. Analyzing azimuth-dependent SWS might help us to better constrain depth-dependent azimuth anisotropy, which might provide better comparisons. But this requires further investigations and is beyond the scope of this study. In addition, we want to highlight that different frequency contents and data sets (teleseismic vs. regional waveforms) are used to extract SWS measurements and azimuthal anisotropy in our study; it is important to acknowledge these data differences when comparing different solutions. Therefore, at the current stage, we are only able to make qualitative instead of quantitative comparisons with other solutions. Another limitation of this study is that we assume that the fast axes align at the horizontal direction; that is, no tilted symmetric cases are allowed. In subduction zones, there might be tilted transverse isotropy induced by descending slabs, and how to extract these tilted symmetric axes from seismic measurements and inversion requires further investigations, especially how to balance the contributions of wave speeds and tilted angles of symmetric axes.

Previous seismological studies have suggested the presence of seismic anisotropy in the transition zone and uppermost lower mantle at both global and regional scales. For instance, in order to reconcile different spherical symmetric Earth's models based on normal mode and body wave travel time tomography, Montagner and Kennett (1996) introduced radial anisotropy within the uppermost and lowermost mantle, as well as in the vicinity of the 660-km discontinuity. Based on Love wave overtune dispersion, Trampert and Heijst (2002) demonstrated the presence of 1% azimuthal anisotropy within the mantle transition zone. Recently, Yuan and Beghein (2013) showed a global feature with strong anisotropy collocated with the 410- and 660-km discontinuities. In addition, based on SWS measurements, Wookey et al. (2002) and Foley and Long (2011) postulated strong mantle flows around the 660-km discontinuity underneath the Tonga subduction zone, which were interpreted as slab-induced anisotropic fabrics.

LPO and shape-preferred orientation (SPO) are the two most likely mechanisms for seismic anisotropy (Karato & Wu, 1995). Mineral physics experiments have demonstrated certain levels of anisotropy for single crystal wadsleyite (Kawazoe et al., 2013; Tommasi et al., 2004; Zha et al., 1997), and hydrous ringwoodite (Kavner, 2003). In addition, magnesiowustite and perovskite, two major minerals within the uppermost lower mantle, might also be intrinsically anisotropic (Karki et al., 1997). Previous studies suggested that dislocation creep is responsible for LPO (Karato et al., 1995). Deformation in the lower mantle is typically considered to be dominated by the diffusion creep, which does not produce strong LPO. Here we argue that large stresses could be induced when the subducting slabs enter the lower mantle, where there is a large jump of viscosity across the 660-km discontinuity (Hager & Richards, 1989; Kusznir, 2000; Mitrovica, 1996; Richard et al., 1992). These large stresses might lead to strain-induced LPO and detectable anisotropy in the subduction region (Ferreira et al., 2019; Wookey et al., 2002). Other causes of observed anisotropy at these depths might involve anisotropic materials entrained by subducted slabs (Wookey et al., 2002), or the presence of oriented melt inclusions (Kendall & Silver, 1998), which cannot be distinguished based on current seismic observations.

5. Conclusion

We jointly interpret wave speed and azimuthal anisotropy features in a new tomographic model (US_{32}), which was developed by combining full waveform inversion and USArray records. Wave speed heterogeneities associated with the descending Juan de Fuca and Gorda slabs and the ascending Yellowstone

plume are consistent with previous tomographic studies. Depth-dependent azimuthal anisotropy observed in this model shed light on the debate about poloidal- and toroidal-mode mantle flows underneath the CSZ. Our new model reveals that poloidal-mode mantle flows dominate the mantle wedge and sub-slab regions at depths shallower than 200 km, in agreement with previous onshore/offshore shear wave splitting measurements. At depths greater than 300 km, two toroidal-mode mantle flows are observed. One surrounds the edge of the Juan de Fuca slab and moves through the slab window around 45°N. The other follows the edge of the Gorda slab and Wyoming downwelling, which enables us to explain the intriguing circular shear wave splitting pattern observed in the Pacific Northwest. In addition, the uppermost lower mantle beneath the Cascadian Subduction Zone is dominated by a northeast-southwest oriented flow field, which might be induced by Farallon Plate subduction over the past 150 Myr. These depth-dependent anisotropic signatures enable us to better characterize complex mantle flow fields underneath the Cascadian Subduction Zone and can be utilized as independent constraints for future physical experiments and numerical flow simulations on subduction-induced mantle flows.

Acknowledgments
We acknowledge the Incorporated Research Institutions for Seismology (IRIS; https://www.iris.edu) for providing observed seismic waveform records and the Texas Advanced Computing Center (TACC; https://www.tacc.utexas.edu) for providing computational resources for this study. The open source spectral-element software package SPECFEM3D_GLOBE and the seismic measurement software package FLEXWIN used in this study are freely available for download via the Computational Infrastructure for Geodynamics (CIG; `geodynamics.org`). This research is supported by NSF Grant EAR-1924282. This is UTD Geoscience contribution number 1367.

References

Atwater, T., & Stock, J. (1998). Pacific-North America plate tectonics of the Neogene south-western United States. *International Geology Review*, *179*, 827–849.

Bird, P. (2003). An updated digital model of plate boundaries. *Geochemistry Geophysics Geosystems*, *4*(3), 1027. https://doi.org/10.1029/2001GC000252

Bodmer, M., Toomey, D., Hooft, E., Nabelek, J., & Braunmiller, J. (2015). Seismic anisotropy beneath the Juan de Fuca plate system: Evidence for heterogeneous mantle flow. *Geology*, *43*, 1095–1098.

Burdick, S., van der Hilst, R., Vernon, F., Martynov, V., Cox, T., Eakins, J., et al. (2013). Model update January 2013: Upper mantle heterogeneity beneath North America from travel-time tomography with global and USArray transportable array data. *Seismological Research Letter*, *85*, 77–81.

Camp, V., & Ross, M. (2004). Mantle dynamics and genesis of mafic magmatism in the intermontane Pacific Northwest. *Journal of Geophysical Research*, *109*, B08204. https://doi.org/10.1029/2003jb002838

Currie, C., Cassidy, J., Hyndman, R., & Bostock, M. (2004). Shear wave anisotropy beneath the Cascadia subduction zone and west North American craton. *Geophysical Journal International*, *157*, 341–353.

Debayle, E., Dubuffet, F., & Durand, S. (2016). An automatically updated S-wave model of the upper mantle and the depth extent of azimuthal anisotropy. *Geophysical Research Letters*, *43*, 674–682. https://doi.org/10.1002/2015GL067329

Dziewonski, A., & Anderson, D. (1981). Preliminary reference Earth model. *Physics of the Earth and Planetary Interiors*, *25*, 297–356.

Eakin, C., Obrebski, M., Allen, R., Boyarko, D., Brudzinksi, M., & Porritt, R. (2010). Seismic anisotropy beneath Cascadia and the Mendocino triple junction: Interaction of the subducting slab with mantle flow. *Earth and Planetary Science Letters*, *297*, 627–632.

Ferreira, A., Faccenda, M., Sturgeon, W., Chang, S., & Schardong, L. (2019). Ubiquitous lower-mantle anisotropy beneath subduction zones. *Nature Geoscience*, *12*, 301–306.

Fichtner, A., Kennett, B., Igel, H., & Bunge, H. (2009). Full seismic waveform tomography for upper-mantle structure in the Australasian region using adjoint methods. *Geophysical Journal International*, *179*, 1703–1725.

Fletcher, R., & Reeves, C. M. (1964). Function minimization by conjugate gradients. *Computer Journal*, *7*, 149–154.

Foley, B., & Long, M. (2011). Upper and mid-mantle anisotropy beneath the Tonga slab. *Geophysical Research Letters*, *38*, L02303. https://doi.org/10.1029/2010GL046021

Ford, M., Grunder, A., & Duncan, R. (2013). Bimodal volcanism of the High Lava Plains and northwestern Basin and Range of Oregon: Distribution and tectonic implications of age-progressive rhyolites. *Geochemistry Geophysics Geosystems*, *14*, 2836–2857. https://doi.org/10.1002/ggge.20175

Gao, H. (2018). Three-dimensional variations of the slab geometry correlate with earthquake distributions at the Cascadia subduction system. *Nature Communications*, *9*, 1204.

Gavin, L., & Lumley, D. (2016). Stress-induced seismic azimuthal anisotropy in the upper crust across the North West Shelf, Australia. *Journal of Geophysical Research: Solid Earth*, *121*, 1023–1039. https://doi.org/10.1002/2015JB012568

Gripp, A., & Gordon, R. (2002). Young tracks of hotspots and current plate velocities. *Geophysical Journal International*, *150*, 321–361.

Hager, B., & Richards, M. (1989). Long-wavelength variations in Earth's geoid: Physical models and dynamical implications. *Philosophical Transactions of the Royal Society B London*, *328*, 309–327.

Hall, C., Fischer, K., & Parmentier, E. (2000). The influence of plate motions on three-dimensional back arc mantle flow and shear wave splitting. *Journal of Geophysical Research*, *105*, 28,009–28,033.

Hawley, W., & Allen, R. (2019). The fragmented death of the Farallon plate. *Geophysical Research Letters*, *46*, 7386–7394. https://doi.org/10.1029/2019GL083437

Hawley, W., Allen, R., & Richards, M. (2016). Tomography reveals buoyant asthenospere accumulating beneath the Juan de Fuca plate. *Science*, *353*, 1406–1408.

Humphreys, E., Schmandt, B., Bezada, M., & Perry-Houts, J. (2015). Recent craton growth by slab stacking beneath Wyoming. *Earth and Planetary Science Letters*, *429*, 170–180.

James, D., Fouch, M., Carlson, R., & Roth, J. (2011). Slab fragmentation, edge flow and the origin of the Yellowstone hotspot track. *Earth and Planetary Science Letters*, *311*, 124–135.

Karato, S., & Wu, P. (1995). Rheology of the upper mantle: A synthesis. *Science*, *260*, 771–778.

Karato, S., Zhang, S., & Wenk, H. (1995). Superplasticity in the Earth's lower mantle: Evidence from seismic anisotropy and rock physics. *Science*, *270*, 458–461.

Karki, B., Stixrude, L., Clark, S., Warren, M., Ackland, G., & Crain, J. (1997). Structure and elasticity of MgO at high pressure. *American Mineralogist*, *82*, 51–60.

Kavner, A. (2003). Elasticity and strength of hydrous ringwoodite at high pressure. *Earth and Planetary Science Letters*, *214*, 645–654.

Kawazoe, T., Ohuchi, T., Nishihara, Y., Nishiyama, N., Fujino, K., & Irifune, T. (2013). Seismic anisotropy in the mantle transition zone induced by shear deformation of wadsleyite. *Physics of the Earth and Planetary Interiors*, *216*, 91–98.

Kendall, J., & Silver, P. (1998). The core-mantle boundary region. In M. Gurnis, M. Wysession, E. Knittle, & B. Buffett (Eds.), *Geodynamics series 28* (pp. 97–118). Washington DC: American Geophysical Union.
King, S., & Anderson, D. (1998). Edge driven convection. *Earth and Planetary Science Letters*, *160*, 280–296.
Komatitsch, D., & Tromp, J. (1999). Introduction to the spectral-element method for 3-D seismic wave propagation. *Geophysical Journal International*, *139*, 806–822.
Kustowski, B., Ekström, G., & Dziewonski, A. (2008). Anisotropic shear-wave velocity structure of the Earth's mantle: A global model. *Journal of Geophysical Research*, *113*, B06306. https://doi.org/10.1029/2007JB005169
Kusznir, N. (2000). Subduction body forces stresses and viscosity structure at the 410 km and 660 km phase transitions. *EOS*, *81*, 1081.
Laske, G., & Masters, G. (1996). Constraints on global phase velocity maps from long-period polarization data. *Journal of Geophysical Research*, *101*, 16,059–16,075.
Lekic, V., Panning, M., & Romanowicz, B. (2010). A simple method for improving crustal correction in waveform tomography. *Geophysical Journal International*, *182*, 265–278.
Levander, A., Schmandt, B., Miller, M., Liu, K., Karlstrom, K., Crow, R. S., et al. (2011). Continuing Colorado plateau uplift by delamination-style convective lithospheric downwelling. *Nature*, *472*, 461–466.
Long, M. (2016). The Cascadia Paradox: Mantle flow and slab fragmentation in the Cascadia subduction system. *Journal of Geodynamics*, *102*, 151–170.
Long, M., & Silver, P. (2008). The subduction zone flow field from seismic anisotropy: A global view. *Science*, *319*, 315–318.
Martin-Short, R., Allen, R., Bastow, I., Totten, E., & Richards, M. (2015). Mantle flow geometry from ridge to trench beneath the Gorda-Juan de Fuca plate system. *Nature Geoscience*, *8*, 965–968.
Mitrovica, J. (1996). Haskell [1935] revisited. *Journal of Geophysical Research*, *101*, 555–569.
Montagner, J. P., Griot-Pommera, D. A., & Lava, J. (2000). How to relate body wave and surface wave anisotropy? *Journal of Geophysical Research*, *105*, 19,015–19,027.
Montagner, J., & Kennett, B. (1996). How to reconcile body-wave and normal-mode reference earth models. *Geophysical Journal International*, *125*, 229–248.
Nelson, P., & Grand, S. (2018). Lower-mantle plume beneath the Yellowstone hotspot revealed by core waves. *Nature Geoscience*, *11*, 280–284.
Obrebski, M., Allen, R., Pollitz, F., & Hung, S. (2011). Lithosphere-asthenosphere interaction beneath the western United States from the joint inversion of body-wave traveltimes and surface-phase velocities. *Geophysical Journal International*, *185*, 1003–1021. https://doi.org/10.1111/j.1365-246X.2011.04990.x
Obrebski, M., Allen, R., Xue, M., & Hung, S. (2010). Slab-plume interaction beneath the Pacific Northwest. *Geophysical Research Letters*, *37*, L14305. https://doi.org/10.1029/2010GL043489
Peter, D., Komatitsch, D., Luo, Y., Martin, R., Goff, L., Casarotti, E., et al. (2011). Forward and adjoint simulations of seismic wave propagation on fully unstructured hexahedral meshes. *Geophysical Journal International*, *186*, 721–739.
Richard, Y., Sabadini, R., & Spada, G. (1992). Isostatic deformations and polar wander induced by redistribution of mass within the Earth. *Journal of Geophysical Research*, *97*, 14,223–14,236.
Russo, R., & Silver, P. (1994). Trench-parallel flow beneath the Nazca plate from seismic anisotropy. *Science*, *263*, 1105–1111.
Savage, M., & Sheehan, A. (2000). Seismic anisotropy and mantle flow from the Great Basin to the Great Plains. *Journal of Geophysical Research*, *105*, 13,715–13,734.
Schaeffer, A., Lebedev, S., & Becker, T. (2016). Azimuthal seismic anisotropy in the Earth's upper mantle and the thickness of tectonic plates. *Geophysical Journal International*, *207*, 901–933.
Schellart, W., Freeman, J., Stegman, D., Moresi, L., & May, D. (2007). Evolution and diversity of subduction zones controlled by slab width. *Nature*, *446*, 308–311.
Schellart, W., Stegman, D., & Freeman, J. (2008). Global trench migration velocities and slab migration induced upper mantle volume fluxes: Constraints to find an Earth reference frame based on minimizing viscous dissipation. *Earth-Science Review*, *88*, 118–144.
Schmandt, B., Dueker, K., Humphreys, E., & Hansen, S. (2012). Hot mantle upwelling across the 660 beneath Yellowstone. *Earth and Planetary Science Letters*, *331*, 224–236.
Schmandt, B., & Humphreys, E. (2010). Complex subduction and small-scale convection revealed by body-wave tomography of the western United States upper mantle. *Earth and Planetary Science Letters*, *297*, 435–445.
Schmandt, B., & Lin, F. (2014). P and S tomography of the mantle beneath the United States. *Geophysical Research Letters*, *41*, 6342–6349. https://doi.org/10.1002/2014GL061231
Shen, W., & Ritzwoller, M. (2016). Crustal and uppermost mantle structure beneath the United States. *Journal of Geophysical Research: Solid Earth*, *121*, 4306–4342. https://doi.org/10.1002/2016JB012887
Sieminski, A., Liu, Q. Y., Trampert, J., & Tromp, J. (2007a). Finite-frequency sensitivity of body waves to anisotropy based upon adjoint methods. *Geophysical Journal International*, *171*, 368–389.
Sieminski, A., Liu, Q. Y., Trampert, J., & Tromp, J. (2007b). Finite-frequency sensitivity of surface wave to anisotropy based upon adjoint methods. *Geophysical Journal International*, *168*, 1153–1174.
Sigloch, K., McQuarrie, N., & Nolet, G. (2008). Two-stage subduction history under North America inferred from multiple-frequency tomography. *Nature Geoscience*, *1*, 458–462.
Silver, P. (1996). Seismic anisotropy beneath the continents: Probing the depths of geology. *Annual Review of Earth and Planetary Sciences*, *24*, 385–432.
Smith, G., Wiens, D., Fischer, K., Dorman, L., Webb, S., & Hildebrand, J. (2001). A complex pattern of mantle flow in the Lau Backarc. *Science*, *292*, 713–716.
Stern, R., & Dumitru, T. (2019). Eocene initiation of the Cascadia subduction zone: A second example of plume-induced subduction initiation? *Geosphere*, *15*, 659–681. https://doi.org/10.1130/GEOS02050.1
Tape, C., Liu, Q., Maggi, A., & Tromp, J. (2009). Adjoint tomography of the southern California crust. *Science*, *325*, 988–992.
Tarantola, A. (1984). Inversion of seismic reflection data in the acoustic approximation. *Geophysics*, *49*, 1259–1266.
Tommasi, A., Mainprice, D., Cordier, P., Thoraval, C., & Couvy, H. (2004). Strain-induced seismic anisotropy of wadsleyite polycrystals and flow patterns in the mantle transition zone. *Journal of Geophysical Research*, *109*, B12405. https://doi.org/10.1029/2004JB003158
Trampert, J., & Heijst, H. (2002). Global azimuthal anisotropy in the transition zone. *Science*, *296*, 1297–1299.
Tromp, J., Tape, C., & Liu, Q. Y. (2005). Seismic tomography, adjoint methods, time reversal and banana-doughnut kernels. *Geophysical Journal International*, *160*, 195–216.
West, J., Fouch, M., Roth, J., & Elkins-Tanton, L. (2009). Vertical mantle flow associated with a lithospheric drip beneath the Great Basin. *Nature Geoscience*, *2*, 439–444.

Wookey, J., Kendall, J., & Barruol, G. (2002). Mid-mantle deformation inferred from seismic anisotropy. *Nature*, *415*, 777–780.
Yuan, K., & Beghein, C. (2013). Seismic anisotropy changes across upper mantle phase transitions. *Earth and Planetary Science Letters*, *374*, 132–144.
Yuan, H., & Dueker, K. (2005). Teleseismic *P*-wave tomogram of the Yellowstone plume. *Geophysical Research Letters*, *32*, L07304. https://doi.org/10.1029/2004GL022056
Yuan, H., Romanowicz, B., Fischer, K., & Abt, D. (2011). 3-D shear wave radially and azimuthally anisotropic velocity model of the North American upper mantle. *Geophysical Journal International*, *184*, 1237–1260.
Zandt, G., & Humphreys, E. (2008). Toroidal mantle flow through the western U.S. slab window. *Geology*, *36*, 295–298.
Zha, C., Duffy, T., Mao, H., Downs, R., Hemley, R., & Weidner, D. (1997). Single-crystal elasticity of β-Mg_2SiO_4 to the pressure of the 410 km seismic discontinuity in the Earth's mantle. *Earth and Planetary Science Letters*, *147*, E9–E15.
Zhang, S., & Karato, S. (1995). Lattice preferred orientation of olivine aggregates deformed in simple shear. *Nature*, *375*, 774–777.
Zhou, Y. (2018). Anomalous mantle transition zone beneath the Yellowstone hotspot track. *Nature Geoscience*, *11*, 449–453.
Zhou, Y., Dahlen, F., & Nolet, G. (2004). Three-dimensional sensitivity kernels for surface wave observables. *Geophysical Journal International*, *158*, 142–168.
Zhou, Q., Liu, L., & Hu, J. (2018). Western US volcanism due to intruding oceanic mantle driven by ancient Farallon slabs. *Nature Geoscience*, *11*, 70–76.
Zhu, H. J., Bozdağ, E., Peter, D., & Tromp, J. (2012). Structure of the European upper mantle revealed by adjoint tomography. *Nature Geoscience*, *5*, 493–498.
Zhu, H., Yang, J., & Li, X. (2020). Azimuthal anisotropy of the North American upper mantle based on full waveform inversion. *Journal of Geophysical Research: Solid Earth*, *125*, e2019JB018432. https://doi.org/10.1029/2019JB018432